



Cite this: DOI: 10.1039/d4nr04877f

Ambipolar conduction in gated tungsten disulphide nanotube

Aniello Pelella,^{*a} Luca Camilli,^{id a} Filippo Giubileo,^{id b} Alla Zak,^c Maurizio Passacantando,^{id d} Yao Guo,^e Kimberly Intonti,^f Arun Kumar^{id f} and Antonio Di Bartolomeo^{id *f}

Devices based on transition metal dichalcogenide nanotubes hold great potential for electronic and opto-electronic applications. Herein, the electrical transport and photoresponse characteristics of a back-gate device with a channel made of a single tungsten disulfide (WS₂) nanotube are investigated as functions of electric stress, ambient pressure, and illumination. As a transistor, the device exhibits p-type conduction, which can be transformed into ambipolar conduction at a high drain–source voltage. Increasing ambient pressure enhances the p-type behaviour, while exposure to light has the opposite effect, enhancing n-type conduction. The ability to operate the device as either a p-type or n-type transistor makes it promising for complementary metal–oxide–semiconductor (CMOS) circuit applications. Light enhances the conductivity, allowing for further control and enabling the device to function as a photodetector with a photoresponsivity of about 50 mA W⁻¹ and a broadband response in the visible range. The combination of voltage, pressure and light control paves the way for using the WS₂ nanotube transistor as a multifunctional device.

Received 20th November 2024,
Accepted 2nd December 2024

DOI: 10.1039/d4nr04877f

rsc.li/nanoscale

1. Introduction

The 2004 isolation of graphene heralded a new era in materials science, sparking a wave of interest in two-dimensional (2D) materials.^{1–6} Among these materials, layered transition metal dichalcogenides (TMDs) have emerged as key players in the field of nanotechnology. TMDs form a class of layered materials with the formula MX₂, where M is a transition metal from groups IV–VIB (Mo, Ti, Nb, W, etcetera) and X is a chalcogen atom (S, Se or Te).^{7,8} These materials have garnered attention for their potential applications in electronics and optoelectronics due to their remarkable physical properties resulting from reduced dimensionality and crystal symmetry.⁹ They have been extensively studied for their layer-dependent properties and optimal application performances.¹⁰ The good gate control and down-scalability have positioned TMDs field-effect transistors (FETs) as promising structures for future electronic

devices.¹¹ Additionally, the controlled synthesis of a few layered TMDs *via* vapor deposition techniques has paved the way for their integration into advanced microchip production.^{12,13}

Among 2D TMDs, tungsten disulphide (WS₂) has garnered attention for its exciting properties and promising performance in various applications, including electronics and optoelectronics.¹⁴ WS₂ exhibits strong spin–orbit coupling, band splitting, and high nonlinear susceptibility.^{15–17} Structurally, WS₂ is a hexagonal layered compound with strong in-plane interactions and weak out-of-plane interactions, resulting in the limited amount of dangling bonds on the layers' edges and inert van der Waals surfaces.^{18,19} This structural feature contributes to its stability and unique properties. The reduced effective electron mass in WS₂ has been predicted to result in the highest mobility and best performance in FETs among 2D TMDs, making it a promising candidate for advanced electronic devices.²⁰ Additionally, WS₂ has shown promise in optoelectronic applications due to its layer-tuneable bandgap and exotic valley physics, making it suitable for light–matter transduction.^{21,22}

One-dimensional (1D) nanotubes (NTs) can offer several advantages over their 2D counterparts. They can enable transistors with smaller size and enhanced gate control through a gate-all-around configuration. More importantly, WS₂ nanotubes exhibit a bulk photovoltaic effect (BPVE) which can be exploited in a new generation of self-powered photodetectors. Indeed, moving from a two-dimensional monolayer to a nano-

^aDipartimento di Fisica, Università di Roma “Tor Vergata”, Via Della Ricerca Scientifica, 00133 Rome, Italy. E-mail: aniello.pelella@uniroma2.it

^bCNR-SPIN Salerno, via Giovanni Paolo II, 84084 Fisciano, Salerno, Italy

^cFaculty of Sciences, Holon Institute of Technology, Holon 58102, Israel

^dDepartment of Physical and Chemical Sciences, University of L'Aquila, 67100 Coppito, L'Aquila, Italy

^eBeijing Institute of Technology, Haidian, Beijing, 100081, China

^fDepartment of Physics “E. R. Caianiello”, University of Salerno, via Giovanni Paolo II, 84084 Fisciano, Salerno, Italy. E-mail: adibartolomeo@unisa.it



tube with polar properties, reduces the crystal symmetry beyond mere broken inversion symmetry of WS₂ and greatly enhances the BPVE.²³ Investigations into the potential of WS₂ NTs have showcased their electromechanical properties even beyond carbon NTs.^{24,25} Indeed, they have been identified as a versatile class of materials with a wide range of potential applications. For instance, WS₂ NTs possess excellent electrochemical performance in lithium-ion batteries.²⁶ Additionally, WS₂ NTs exhibit high performance as photodetectors for visible and near-infrared light, positioning them as promising candidates for nanoscale optoelectronics.²⁷ Moreover, their significant bulk photovoltaic effect, particularly in the infrared region, could have implications for advanced photovoltaic applications.^{23,28}

The synthesis of WS₂ NTs has been explored using various methods.^{25,29,30} WS₂ NTs with small diameters and few walls are crucial for understanding their distinct characteristics.^{31,32} Indeed, studies have explored the optical properties of WS₂ NTs, revealing that a decrease in NT diameter induces a red-shift in photoluminescence, suggesting a narrowed band gap due to a curvature and strain effect.³³ In another study, the cathodoluminescence of WS₂ NTs with different diameters and amount of layers was investigated and compared to literature results. Here, the red shift of all types NTs vs. bulk WS₂ was attributed to the compatible effect between the quantum confinement (blue shift) in c-direction due to reduction of number of layers to single layer and strain promoted red shift.³⁴ Recent studies have also focused on the functionalization of tungsten disulfide (WS₂) NTs with various materials to enhance their properties for specific applications, such as fluorescence and conductivity.^{35,36}

However, FETs based on individual WS₂ NT have not been extensively explored, compared to their 2D WS₂-based counterparts.^{14,37} Notably, the pioneering work by R. Levi *et al.* in 2013 introduced the first FET³⁸ utilizing a single WS₂ NT, with limited subsequent studies reported. In this context, we have recently reported an individual multi-walled WS₂ NT which has been utilized as a channel of a back-gated FET, exhibiting p-type behaviour in ambient conditions and low bias, with a hole mobility $\mu_p \sim 1.4 \text{ cm}^2 \text{ V}^{-1} \text{ s}^{-1}$ and a subthreshold swing $SS \sim 10 \text{ V dec}^{-1}$.³⁹

In this work, we synthesized WS₂ NTs through a two-step reaction process and spread them onto a Si/SiO₂ substrate.³⁰ With the help of scanning electron microscopy (SEM), we determined the position of single NTs and contacted them using electron beam lithography. This device is a FET with p-type behaviour at low bias and ambient conditions, and conductance that can be tuned by ambient pressure. For consistency, all the data reported herein refer to the same device. However, we fabricated several devices in the same batch, which showed similar behaviour.³⁹

Most importantly, we demonstrate that the device can switch from hole-dominant to electron-dominant conduction, *i.e.* it exhibits an ambipolar behaviour, at a drain-source voltage bias higher than about 1 V. Ambipolar devices, capable of functioning as both n-type and p-type transistors by adjust-

ing the bias, offer flexibility in logic and analog circuit design.^{40–42} Incorporating ambipolar transistors in CMOS (complementary metal-oxide-semiconductor) circuits enables the implementation of more complex logic functions per chip, thereby enhancing the computational capabilities of integrated circuits.

Furthermore, the device can be operated as a photodetector in the visible range, with a responsivity peak around 1.9 eV, correlated with WS₂ indirect band gap value. The control by electric bias, pressure and light can make WS₂ NT based transistors versatile devices in several applications.

2. Results and discussion

The schematic of the device under study is displayed in Fig. 1(a). A single WS₂ NT serves as the channel of the FET, where drain and source contacts are formed by titanium/gold (Ti/Au) metal pads. The channel current (I_d) can be modulated by the voltage applied to the gate terminal (V_{gs}) located at the back of the p-silicon substrate.

Transmission electron microscopy (TEM) was performed to check the structure of the NT and measure its radius. From the TEM image reported in Fig. 1b, we estimated the NT outer radius to be $r = 17 \text{ nm}$, which is in the range of the average dimensions for NTs obtained through the same fabrication process (see Experimental section).³⁹ Here the interlayer distance in NTs' walls is of 0.63 nm, $\sim 1.6\%$ larger than that of bulk WS₂ (0.62 nm), which was assigned to strain in the rolled layers.³⁴

Electrical characterization of the device was performed under dark and high vacuum conditions ($p = 1 \times 10^{-4} \text{ mbar}$). The I_d - V_{ds} output characteristic, *i.e.* the measurement of the channel current *versus* the applied drain-source voltage V_{ds} , at $V_{gs} = 0 \text{ V}$, displayed in Fig. 1(c), reveals a slightly asymmetric Schottky behaviour which can be due to a small difference in the junction areas between NT and source/drain contacts.^{43–45} The I_d - V_{gs} transfer characteristic at $V_{ds} = 0.25 \text{ V}$ in Fig. 1(d) reveals a hysteretic p-type conduction. The hysteretic behaviour reported in the transfer characteristic of the device is due to intrinsic defects and the presence of O₂ and H₂O on the NT surface that induce slow-time charge trapping, thus enlarging the difference between the forward and the reverse sweep curve.⁴⁶ From the transfer characteristic, we estimate the hole mobility using the following formula:

$$\mu_h = g_{m,\max} \frac{L}{C_{\text{ox}} V_{ds}} \quad (1)$$

where $g_{m,\max}$ is the maximum transconductance, $L = 10 \mu\text{m}$ is the length of the NT, $C_{\text{ox}} = 13.5 \times 10^{-12} \text{ F m}^{-1}$ is the oxide capacitance per unit length (the method for evaluating C_{ox} is reported elsewhere^{47–50}). The analysis yields a hole mobility $\mu_p = 0.54 \text{ cm}^2 \text{ V}^{-1} \text{ s}^{-1}$, which corresponds to a hole density $p = \frac{J}{ev_d} = \frac{JL}{e\mu_p V_{ds}} = 2.2 \times 10^3 \text{ cm}^{-3}$, where J is the current density and v_d the carrier drift velocity.



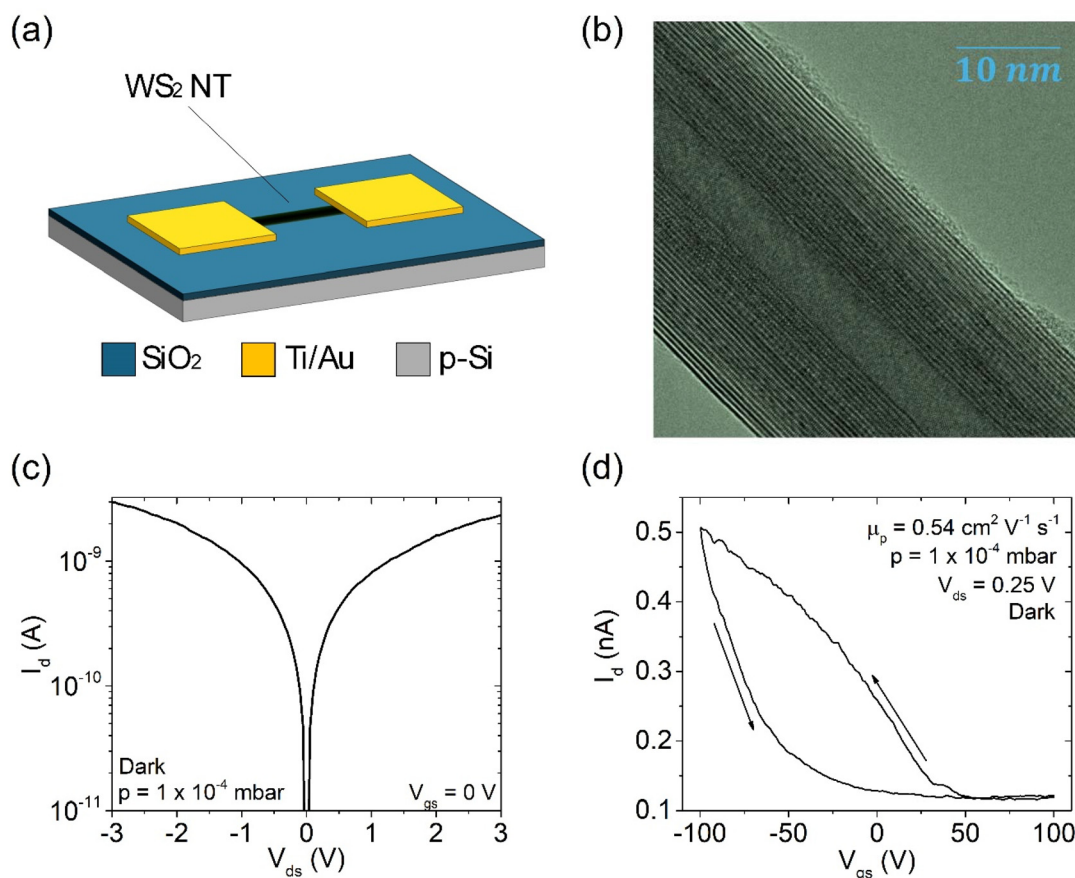


Fig. 1 (a) Schematic of the WS₂ NT device in back gate configuration. (b) TEM image of a typical WS₂ NT. (c) Output (I_d - V_{ds}) and (d) transfer (I_d - V_{gs}) characteristics of the WS₂ NT transistor in dark and high vacuum conditions.

To complete the FET electrical characterization in high vacuum, we measured several I_d - V_{ds} characteristics at different applied V_{gs} (Fig. 2a). V_{gs} varies in the range ± 100 V, with a step of 10 V. Fig. 2a shows different behaviours between forward and reverse branches. Indeed, at high positive V_{ds} , the drain current suddenly increases for $V_{gs} > 30$ V. This is clearly shown

in the plot of Fig. 2b that reports the current at $V_{ds} = \pm 3$ V. The black curve in Fig. 2b reveals that the WS₂ NT transistor has an ambipolar behaviour at $V_{ds} = +3$ V, while the conduction is clearly dominated by holes at negative $V_{ds} = -3$ V, for which the transfer characteristic is p-type (red curve in Fig. 2b). We note that, at $V_{ds} = +3$ V, the n -branch at positive V_{gs} becomes

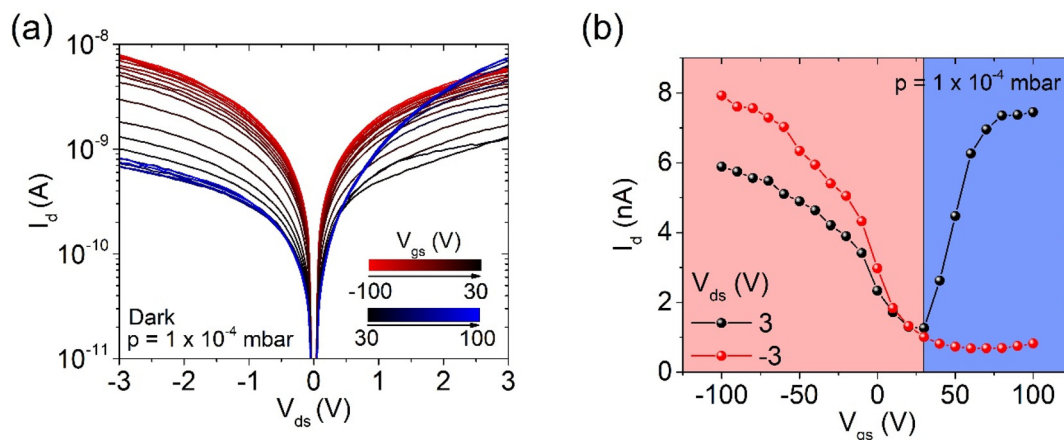


Fig. 2 (a) Output characteristics in dark and high vacuum conditions. (b) Current values extracted at ± 3 V from data in (a).



higher than the p-branch at negative V_{gs} , resulting in a complete switching from a p-type to a dominant n-type conduction.

With the aim to investigate the ambipolar conduction of the WS_2 NT FET, we further studied the transistor properties at positive V_{ds} . Fig. 3a reports the transfer characteristics of the device at different positive V_{ds} , from 0.25 V to 3.00 V, with a step of 0.25 V. The data show that, starting from a p-type

device, the increase in V_{ds} activates electron conduction, thus enabling ambipolarity. Fig. 3b shows that, while hole mobility stays constant, the electron mobility increases with V_{ds} . Indeed, switching from p-type conduction to dominant n-type conduction occurs at about $V_{ds} = 1.25$ V, where electron mobility overcomes hole mobility.

Fig. 3c shows the transfer characteristics of the device measured at different V_{gs} ranges, from ± 20 V to ± 100 V, at a

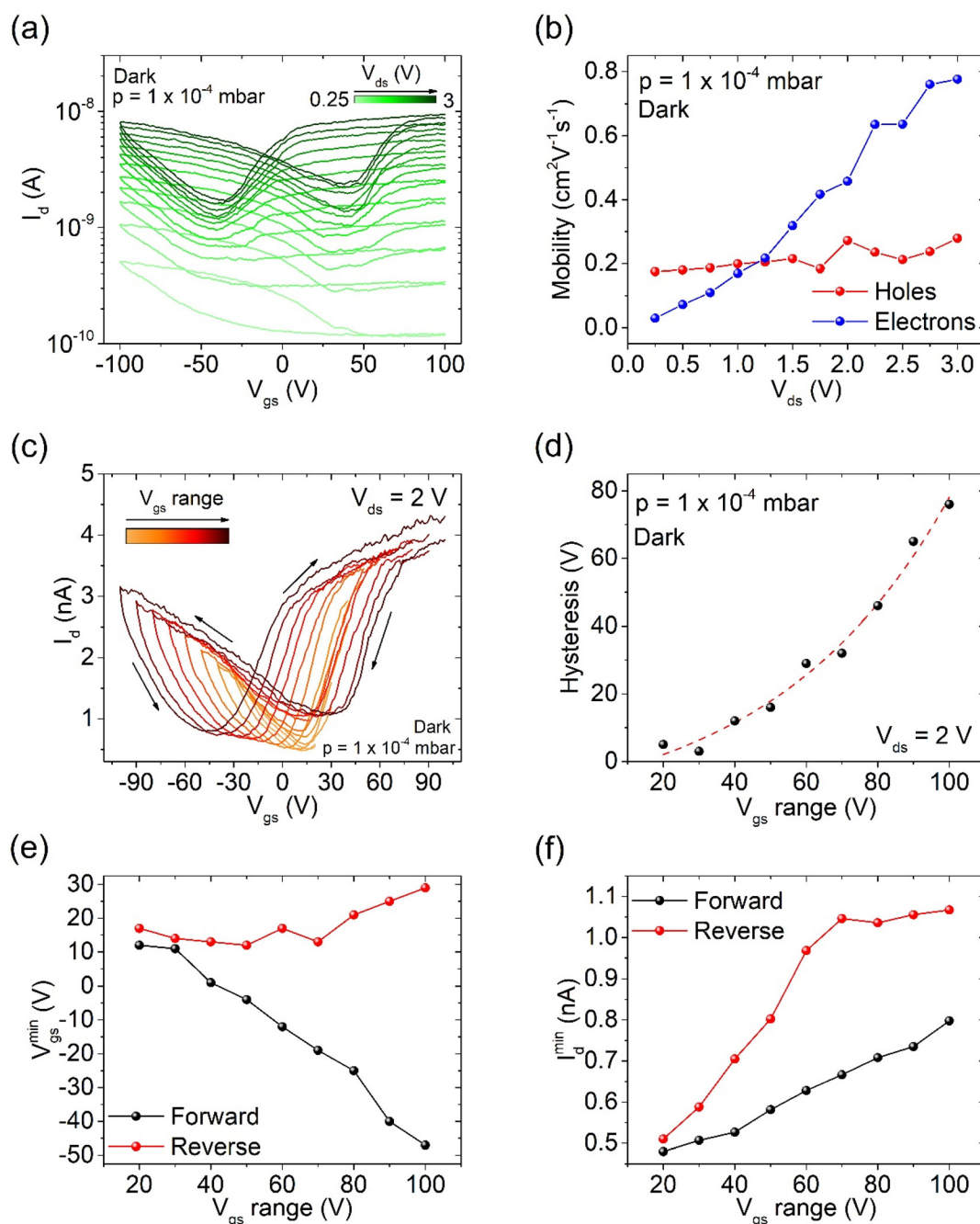


Fig. 3 (a) Transfer characteristics at different V_{ds} in high vacuum. (b) Mobility extracted from $g_{m,max}$ evaluated in the reverse branch of the transfer characteristics in (a). (c) Transfer characteristics with different V_{gs} range in high vacuum. (d) Hysteresis versus applied V_{gs} range, extracted from data in (c). (e) Gate voltage V_{gs}^{min} and (f) minimum current I_d^{min} as a function of V_{gs} , for the forward and reverse sweep.



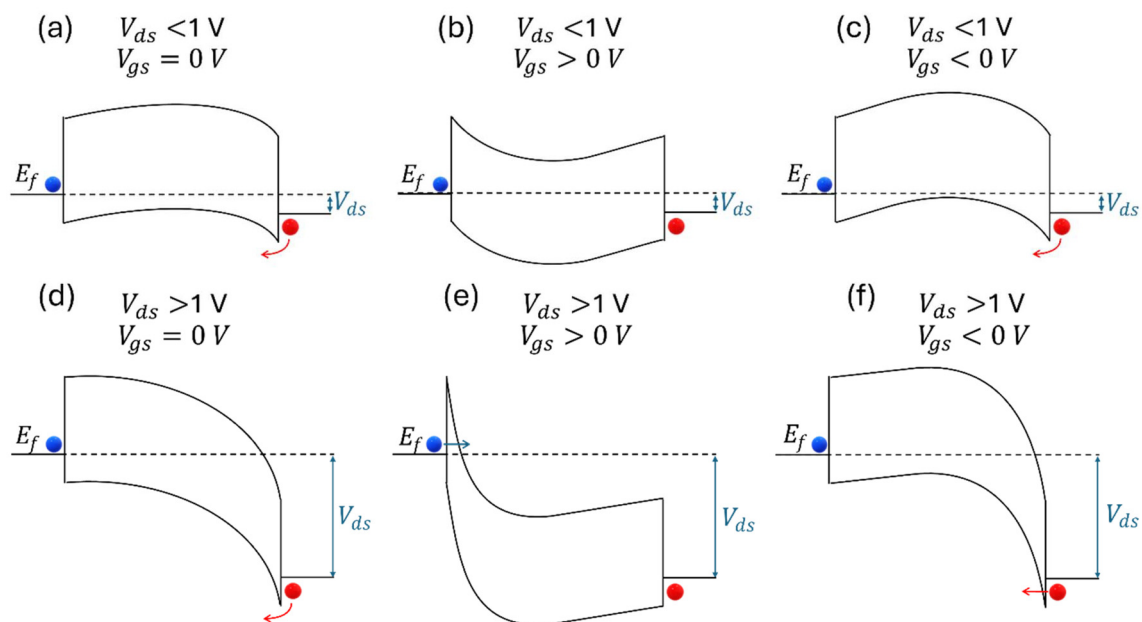


Fig. 4 Band diagram model at (a–c) low and (d–f) high V_{ds} voltage bias for different applied V_{gs} .

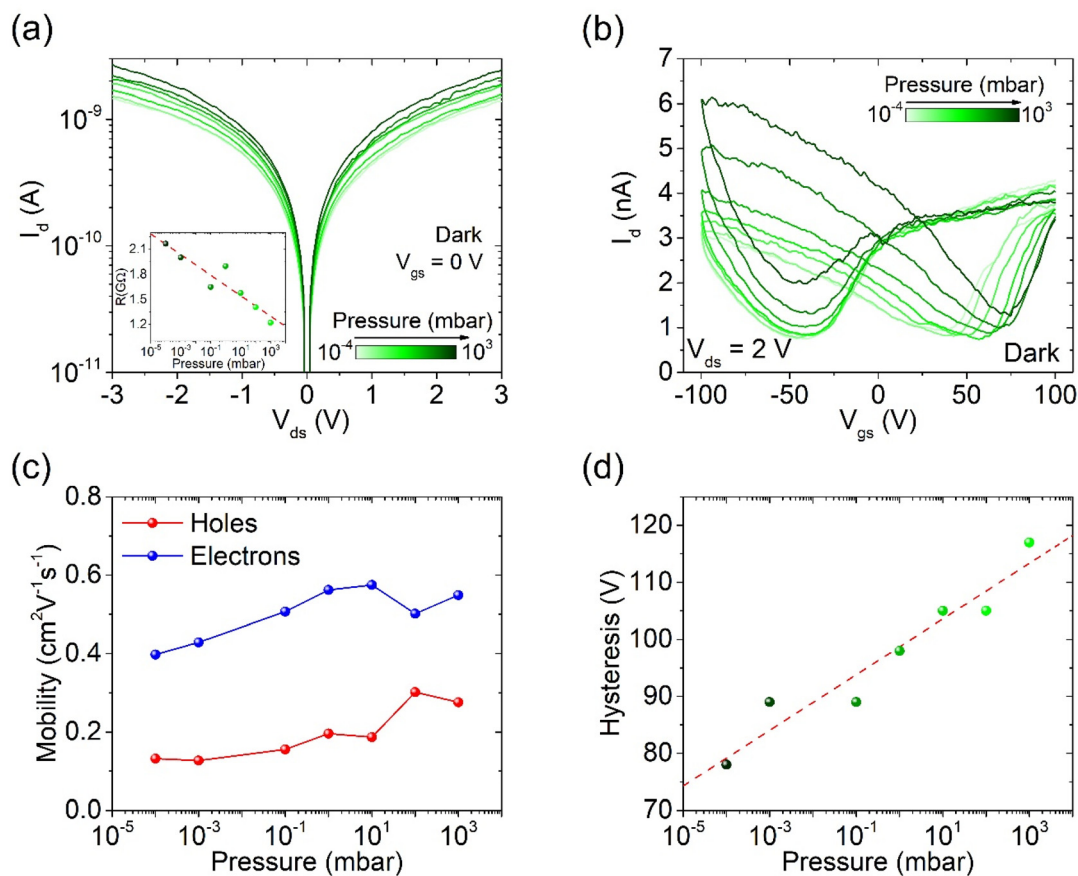


Fig. 5 (a) I – V curves at different pressures. Inset: resistance as a function of the pressure. (b) Transfer characteristics at different pressures. (c) Charge carrier mobility and (d) hysteresis width versus pressure.



fixed $V_{ds} = 2$ V. To correctly evaluate the effect of the different V_{gs} ranges, we define the hysteresis H as the difference of V_{gs}^{min} , *i.e.* the voltage at which I_d is minimum (I_d^{min}), in reverse and forward voltage sweeps. H versus V_{gs} is plotted in Fig. 3d. The increase in the hysteresis with V_{gs} range is due to the increasing carrier trapping at the WS₂ NT/SiO₂ interface, due to the longer sweeping time.^{41,51–53} The left-shift of V_{gs}^{min} during the forward sweep is stronger compared to the right-shift that occurs during the reverse sweep (Fig. 3e) and indicates that

hole trapping is more effective than electron trapping.^{54,55} Furthermore, the increasing V_{gs} range and measurement time also leads to an overall increase in current, as reported in Fig. 3c and highlighted in Fig. 3f, where the minimum values of the current are plotted *versus* V_{gs} range.

The observed behaviour can be explained by the band diagram model described in Fig. 4. WS₂ is a p-type semiconductor, hence the Fermi level (E_f) is close to the valence band, as demonstrate also by XPS.²⁵ Also, the work function of

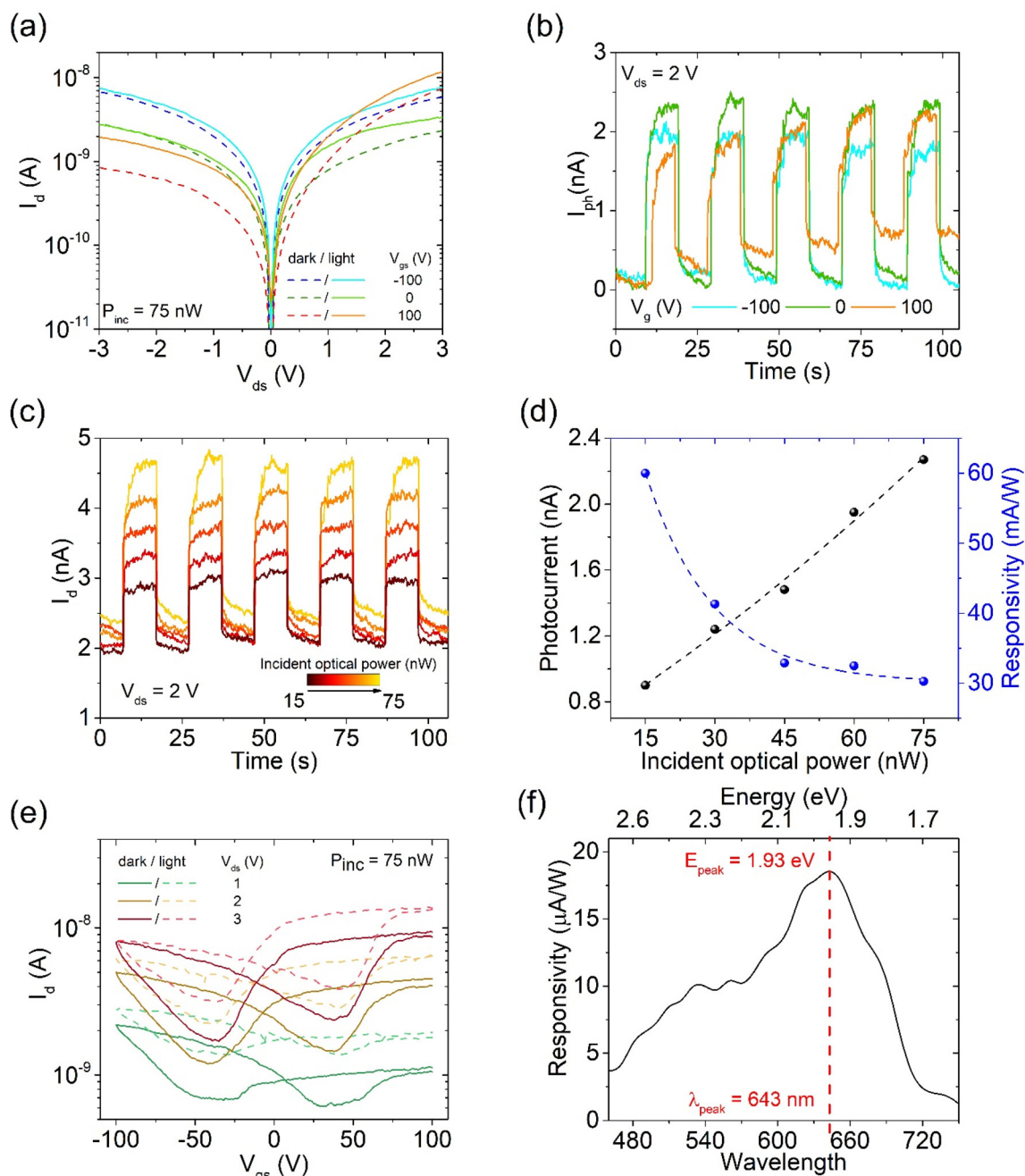


Fig. 6 (a) Output curves at different V_{gs} in dark and under illumination. (b) Transient photocurrent at different V_{gs} and (c) at different incident optical power. (d) Photocurrent and responsivity versus incident optical power. (e) Transfer characteristics at different V_{ds} in dark and under illumination. (f) Responsivity versus wavelength/energy of the incident laser beam.



WS₂ is around 5.1 eV and is higher than the titanium work function, which is 4.33 eV.^{25,56} These considerations lead to Fig. 4a, which shows the band diagram when low $V_{ds} < 1$ V and $V_{gs} = 0$ V are applied. In this scenario, a very low current, only due to the holes that can overcome the barrier at the drain contact, flows through the FET channel. When V_{gs} increases (Fig. 4b), the bands bend downwards, further blocking the migration of holes. In contrast, when a negative V_{gs} is applied, the bands bend upwards favouring the flow of holes through the channel (Fig. 4c). This explains the p-type conduction of the devices observed at low drain voltage.

On the other hand, when a high $V_{ds} > 1$ V is applied, the switching of V_{gs} from negative to positive values enables ambipolar conduction. Indeed, when $V_{gs} = 0$ V, holes can overcome the drain barrier, generating a p-type current (Fig. 4d). At positive V_{gs} , the bands bend downward, suppressing hole injection from the drain; however, the simultaneous thinning of the electron barrier at the source enables electron tunnelling, which is responsible for the emergence of a n-type current (Fig. 4e). Finally, at negative V_{gs} , hole conduction is favoured by the upward bending of the bands (Fig. 4f).

Increasing ambient pressure to standard conditions exposes the WS₂ NT to molecules such as oxygen and water. These molecules act as p-dopants when adsorbed on the surface of the NT. This results in an increase in hole density, *i.e.* of the channel conductance, and a slight change in the shape of the output and transfer characteristics of the device. The output (Fig. 5a) and transfer characteristics (Fig. 5b) measured at different pressures, from $p = 1 \times 10^{-4}$ mbar to standard ambient conditions ($p = 1 \times 10^3$ mbar), confirm the expected trend. Output characteristics reveal a resistance linear behaviour, which decreases with increasing pressure, as highlighted in the inset of Fig. 5a.

Electron and hole mobilities have been estimated and reported in Fig. 5c. The charge carrier mobilities are almost constant in the investigated range (that is, 7 orders of magnitude), hence they do not vary significantly with the pressure. Finally, Fig. 5d shows the enhancement of the hysteresis at high pressure, where the concentration of O₂ and H₂O molecules increases.

We also investigated the effect of light on the WS₂ NT FET properties, in high vacuum conditions. To this purpose, we exposed the NT to light from a supercontinuum laser. The laser beam has a nominal maximum output power $P = 110$ mW, which, scaled by the illuminated area of the NT and the laser spot ($A_{spot} = 25 \times 10^{-4}$ cm²), results in an incident optical power $P_{inc} = 80$ nW. Fig. 6a shows the output curves in dark and under laser illumination at different applied V_{gs} . In particular, at negative V_{ds} , the effect of illumination is negligible at zero and negative high V_{gs} , while there is an appreciable photocurrent for high positive V_{gs} . This is due to the dominant p-type conduction for $V_{ds} < 0$, as already commented above. At positive V_{ds} , ambipolar conduction occurs and photoresponse varies for different V_{gs} . Fig. 6b reports the photocurrent I_{ph} (defined as the difference between light and dark current) peaks at different V_{gs} . Different photoresponse

($V_{ds} = 2$ V) occurs for different V_{gs} . The best performances are obtained for $V_{gs} = 0$ V, for which the highest response and the lower dark current are reported.

To further test the device as a photodetector, we changed the power of the laser beam while measuring the current flowing into the channel. The results are shown in Fig. 6c, where $V_{ds} = 2$ V and $V_{gs} = 0$ V, while P_{inc} varies from 15 to 75 nW. I_{ph} and the responsivity R (defined as $R = I_{ph}/P_{inc}$) are extracted from Fig. 6c and plotted against P_{inc} in Fig. 6d. Higher responsivity is reported at lower incident power, along with a photocurrent that increases with increasing P_{inc} . The increasing illumination power leads to an increase in photo-generated charge carriers, which corresponds to an increase in photocurrent. However, at high incident optical power, the enhanced carrier density leads to an increase in the scattering rate favouring electron–hole recombination and limiting the charge carrier mobility, thus resulting in a low responsivity.^{57,58}

Moreover, transfer characteristics at different V_{ds} have been measured in the dark and under illumination (Fig. 6e). The incidence of the laser on the NT favours the desorbing of oxygen molecules from the surface, due to local heating, thus enhancing conduction by electrons, *i.e.* reversing the atmospheric p-doping effect.^{59,60}

The responsivity as a function of the light wavelength is displayed in Fig. 6f. The peak at $\lambda_{peak} = 643$ nm ($E_{peak} = 1.93$ eV) falls within the range of energy band gaps of WS₂ NTs.^{61,62}

3. Conclusion

We have investigated the electrical and optical properties of a single tungsten disulphide nanotube field effect transistor. We observed an ambipolar conduction that can be tuned by drain voltage, pressure and light. The transistor can switch from p-type to n-type conduction by increasing the drain–source voltage bias. We also demonstrated that the device can function as a photodetector with a good photoresponse in the visible range. The tuneable ambipolar conduction and photoconduction make the device promising for CMOS-integrated optoelectronic circuits.

4. Materials and methods

The synthesis of multiwall WS₂ nanotubes consisted in few steps.³⁰ Here, *via* a reduction–sulfurization process, the initially grown tungsten suboxide nanowhiskers were transformed into WS₂ nanotubes. The process is a one-pot synthesis, which means that both reactions (growth of oxide nanowhiskers and their sulfurization into WS₂ NTs) occurred in the same reactor, under identical conditions (same elevated temperature, same H₂S, H₂ and N₂ flows), and followed one another in a self-regulated manner. The nanowhiskers were synthesized through a series of intermediate reduction reactions from a blend of various WO_x ($2.83 \leq x \leq 3$) suboxide phases



and shapes. The process first included the reduction of the precursor into a volatile suboxide phase W_4O_{11} ($WO_{2.75}$), and its evaporation, further partial reduction of the $WO_{2.75}$ vapor into WO_2 , and finally the “chemical” condensation of the vapor mixture into 1D nanocrystals giving the formation of a stable against additional reduction $W_{18}O_{49}$ suboxide phase. These suboxide nanowhiskers were then transformed into WS_2 nanotubes, starting from the surface and moving inward, towards the inner core through a slow diffusion-controlled sulfurization reaction.

The WS_2 nanotubes were then spread onto a Si/SiO₂ (tox = 500 nm) wafer, and their locations were determined using optical microscopy. Electrodes were created using electron beam lithography and electron beam evaporation of Ti/Au (20/120 nm) followed by a lift-off process in acetone.

The TEM sample characterization was performed with an FEI Tecnai G2 F20.

For the opto-electronic characterization, the device was tested in a Lakeshore probe-station with integrated optical fiber, connected to a Keithley Parameter Analyzer 4200-SCS. The pressure chamber was controlled by two external pumps (rotative and turbomolecular) and a needle valve.

The white laser source was a NKT Photonics Supercontinuum Laser (450–2400 nm) (SuperK COMPACT), with a nominal output power $P = 110$ mW and spectrum in the range 450–2400 nm.

4.1. Statistical analysis

All statistical analyses were performed using OriginLab software. We did not perform any pre-processing of the data, such as transformation, normalization, or evaluation of outliers.

Data availability

The data that support the findings of this study are available from the corresponding author upon reasonable request.

Conflicts of interest

There are no conflicts to declare.

Acknowledgements

This work is supported by the Science for Peace and Security (SPS) Programme, NATO Emerging Security Challenges Division, project SPS G5936, Ultralight Wearable Solar Cells as a Portable Electricity source (ESCAPE).

References

- C.-H. Yeh, Y.-T. Chen and D.-W. Hsieh, *RSC Adv.*, 2021, **11**, 33276–33287.
- F. Urban, G. Lupina, A. Grillo, N. Martucciello and A. Di Bartolomeo, *Nano Express*, 2020, **1**, 010001.
- A. Longo, A. Di Bartolomeo, E. Faella, A. Pelella, F. Giubileo, A. Sorrentino, M. Palomba, G. Carotenuto, G. Barucca, A. Tagliaferro and U. Coscia, *Coatings*, 2022, **12**, 1446.
- A. Pelella, A. Grillo, E. Faella, G. Luongo, M. B. Askari and A. Di Bartolomeo, *ACS Appl. Mater. Interfaces*, 2021, **13**, 47895–47903.
- A. Grillo, Z. Peng, A. Pelella, A. Di Bartolomeo and C. Casiraghi, *ACS Nano*, 2023, **17**, 1533–1540.
- F. Giubileo, D. Capista, E. Faella, A. Pelella, W. Y. Kim, P. Benassi, M. Passacantando and A. Di Bartolomeo, *Adv. Electron. Mater.*, 2023, **9**, 2200690.
- T. Chowdhury, E. C. Sadler and T. J. Kempa, *Chem. Rev.*, 2020, **120**, 12563–12591.
- S. Tajik, Z. Dourandish, F. Garkani Nejad, H. Beitollahi, P. M. Jahani and A. Di Bartolomeo, *Biosens. Bioelectron.*, 2022, **216**, 114674.
- G. Wang, A. Chernikov, M. M. Glazov, T. F. Heinz, X. Marie, T. Amand and B. Urbaszek, *Rev. Mod. Phys.*, 2018, **90**, 021001.
- C. Tan, Z. Lai and H. Zhang, *Adv. Mater.*, 2017, **29**, 1701392.
- A. Liu, X. Zhang, Z. Liu, Y. Li, X. Peng, X. Li, Y. Qin, C. Hu, Y. Qiu, H. Jiang, Y. Wang, Y. Li, J. Tang, J. Liu, H. Guo, T. Deng, S. Peng, H. Tian and T.-L. Ren, *Nano-Micro Lett.*, 2024, **16**, 119.
- Y. Shi, H. Li and L.-J. Li, *Chem. Soc. Rev.*, 2015, **44**, 2744–2756.
- Z. Peng, A. Grillo, A. Pelella, X. Liu, M. Boyes, X. Xiao, M. Zhao, J. Wang, Z. Hu, A. D. Bartolomeo and C. Casiraghi, *Mater. Horiz.*, 2024, **11**, 1344–1353.
- A. Pelella, K. Intonti, O. Durante, A. Kumar, L. Viscardi, S. De Stefano, P. Romano, F. Giubileo, H. Neill, V. Patil, L. Ansari, B. Roycroft, P. K. Hurley, F. Gity and A. Di Bartolomeo, *Discover Nano*, 2024, **19**, 57.
- Y. Yue, J. Chen, Y. Zhang, S. Ding, F. Zhao, Y. Wang, D. Zhang, R. Li, H. Dong, W. Hu, Y. Feng and W. Feng, *ACS Appl. Mater. Interfaces*, 2018, **10**, 22435–22444.
- A. Srivastava, M. Sidler, A. V. Allain, D. S. Lembke, A. Kis and A. Imamoglu, *Nat. Phys.*, 2015, **11**, 141–147.
- S. Wang, S. Li, T. Chervy, A. Shalabney, S. Azzini, E. Orgiu, J. A. Hutchison, C. Genet, P. Samorì and T. W. Ebbesen, *Nano Lett.*, 2016, **16**, 4368–4374.
- H. L. Zhu, C. J. Zhou, B. S. Tang, W. F. Yang, J. W. Chai, W. L. Tay, H. Gong, J. S. Pan, W. D. Zou, S. J. Wang and D. Z. Chi, *Appl. Phys. Lett.*, 2018, **112**, 171604.
- D. Bocharov, S. Piskunov, Y. F. Zhukovskii and R. A. Evarestov, *Phys. Status Solidi RRL*, 2019, **13**, 1800253.
- M. Liu, S. Wei, S. Shahi, H. N. Jaiswal, P. Paletti, S. Fathipour, M. Remškar, J. Jiao, W. Hwang, F. Yao and H. Li, *Nanoscale*, 2020, **12**, 17253–17264.
- S. Tongay, J. Zhou, C. Ataca, J. Liu, J. S. Kang, T. S. Matthews, L. You, J. Li, J. C. Grossman and J. Wu, *Nano Lett.*, 2013, **13**, 2831–2836.



- 22 I. Paradisanos, S. Germanis, N. T. Pelekanos, C. Fotakis, E. Kymakis, G. Kioseoglou and E. Stratakis, *Appl. Phys. Lett.*, 2017, **110**, 193102.
- 23 Y. J. Zhang, T. Ideue, M. Onga, F. Qin, R. Suzuki, A. Zak, R. Tenne, J. H. Smet and Y. Iwasa, *Nature*, 2019, **570**, 349–353.
- 24 R. Levi, J. Garel, D. Teich, G. Seifert, R. Tenne and E. Joselevich, *ACS Nano*, 2015, **9**, 12224–12232.
- 25 A. Grillo, M. Passacantando, A. Zak, A. Pelella and A. Di Bartolomeo, *Small*, 2020, **16**, 2002880.
- 26 J. Zhang, H. Sade, Y. Zhao, A. T. Murdock, A. Bendavid, J.-P. Lellouche, G. Wang and Z. Han, *Nanotechnology*, 2018, **30**, 035401.
- 27 A. Yu. Polyakov, L. Yadgarov, V. Lebedev, R. G. Chumakov, L. V. Yashina, M. N. Rumyantseva, R. Tenne and E. A. Goodilin, *AIP Conf. Proc.*, 2021, **2359**, 020025.
- 28 B. Kim, N. Park and J. Kim, *Nat. Commun.*, 2022, **13**, 3237.
- 29 J. Chen, S.-L. Li, F. Gao and Z.-L. Tao, *Chem. Mater.*, 2003, **15**, 1012–1019.
- 30 P. Chithaiah, S. Ghosh, A. Idelevich, L. Rovinsky, T. Livneh and A. Zak, *ACS Nano*, 2020, **14**, 3004–3016.
- 31 Y. Yomogida, Y. Miyata and K. Yanagi, *Appl. Phys. Express*, 2019, **12**, 085001.
- 32 V. Brüser, R. Popovitz-Biro, A. Albu-Yaron, T. Lorenz, G. Seifert, R. Tenne and A. Zak, *Inorganics*, 2014, **2**, 177–190.
- 33 M. A. Rahman, Y. Yomogida, A. Ahad, K. Ueji, M. Nagano, A. Ihara, H. Nishidome, M. Omoto, S. Saito, Y. Miyata, Y. Gao, S. Okada and K. Yanagi, *Sci. Rep.*, 2023, **13**, 16959.
- 34 S. Ghosh, V. Brüser, I. Kaplan-Ashiri, R. Popovitz-Biro, S. Peglow, J. I. Martínez, J. A. Alonso and A. Zak, *Appl. Phys. Rev.*, 2020, **7**, 041401.
- 35 V. B. Kumar, Y. Harel, R. Ben-Ishay, J.-P. Lellouche and A. Gedanken, *Macromol. Chem. Phys.*, 2019, **220**, 1800476.
- 36 Q. Palomar, C. Gondran, J.-P. Lellouche, S. Cosnier and M. Holzinger, *J. Mater. Chem. B*, 2020, **8**, 3566–3573.
- 37 N. A. N. Phan, H. Noh, J. Kim, Y. Kim, H. Kim, D. Whang, N. Aoki, K. Watanabe, T. Taniguchi and G. Kim, *Small*, 2022, **18**, 2105753.
- 38 R. Levi, O. Bitton, G. Leitus, R. Tenne and E. Joselevich, *Nano Lett.*, 2013, **13**, 3736–3741.
- 39 A. Pelella, A. Kumar, K. Intonti, O. Durante, S. De Stefano, X. Han, Z. Li, Y. Guo, F. Giubileo, L. Camilli, M. Passacantando, A. Zak and A. Di Bartolomeo, *Small*, 2024, 2403965.
- 40 X. Li, P. Zhou, X. Hu, E. Rivers, K. Watanabe, T. Taniguchi, D. Akinwande, J. S. Friedman and J. A. C. Incorvia, *ACS Nano*, 2023, **17**, 12798–12808.
- 41 A. Di Bartolomeo, A. Pelella, X. Liu, F. Miao, M. Passacantando, F. Giubileo, A. Grillo, L. Iemmo, F. Urban and S.-J. Liang, *Adv. Funct. Mater.*, 2019, **29**, 1902483.
- 42 M. Sugahara, H. Kawai, Y. Yomogida, Y. Maniwa, S. Okada and K. Yanagi, *Appl. Phys. Express*, 2016, **9**, 075001.
- 43 W. Gao, S. Zhang, F. Zhang, P. Wen, L. Zhang, Y. Sun, H. Chen, Z. Zheng, M. Yang, D. Luo, N. Huo and J. Li, *Adv. Electron. Mater.*, 2021, **7**, 2000964.
- 44 A. Di Bartolomeo, A. Grillo, F. Urban, L. Iemmo, F. Giubileo, G. Luongo, G. Amato, L. Croin, L. Sun, S.-J. Liang and L. K. Ang, *Adv. Funct. Mater.*, 2018, **28**, 1800657.
- 45 A. Grillo and A. Di Bartolomeo, *Adv. Electron. Mater.*, 2021, **7**, 2000979.
- 46 W. Kim, A. Javey, O. Vermesh, Q. Wang, Y. Li and H. Dai, *Nano Lett.*, 2003, **3**, 193–198.
- 47 L. Viscardi, E. Faella, K. Intonti, F. Giubileo, V. Demontis, D. Prete, V. Zannier, L. Sorba, F. Rossella, P. Romano and A. D. Bartolomeo, in *2023 IEEE Nanotechnology Materials and Devices Conference (NMDC)*, IEEE, Paestum, Italy, 2023, pp. 773–777.
- 48 O. Wunnicke, *Appl. Phys. Lett.*, 2006, **89**, 083102.
- 49 V. Demontis, D. Prete, E. Faella, F. Giubileo, V. Zannier, O. Durante, L. Sorba, A. Di Bartolomeo and F. Rossella, *Nano Express*, 2024, **5**, 035007.
- 50 D. R. Khanal and J. Wu, *Nano Lett.*, 2007, **7**, 2778–2783.
- 51 A. Di Bartolomeo, L. Genovese, F. Giubileo, L. Iemmo, G. Luongo, T. Foller and M. Schleberger, *2D Mater.*, 2017, **5**, 015014.
- 52 T. Knobloch, G. Rzepa, Y. Yu. Illarionov, M. Walzl, F. Schanovsky, B. Stampfer, M. M. Furchi, T. Mueller and T. Grasser, *IEEE J. Electron Devices Soc.*, 2018, **6**, 972–978.
- 53 C. Lan, X. Kang, Y. Meng, R. Wei, X. Bu, S. Yip and J. C. Ho, *Nano Res.*, 2020, **13**, 3278–3285.
- 54 X. Ma, Y.-Y. Liu, L. Zeng, J. Chen, R. Wang, L.-W. Wang, Y. Wu and X. Jiang, *ACS Appl. Mater. Interfaces*, 2022, **14**, 2185–2193.
- 55 P.-S. Liu, C.-T. Lin, B. Hudec and T.-H. Hou, *Nanotechnology*, 2017, **28**, 475204.
- 56 A. Voldman, D. Zbaida, H. Cohen, G. Leitus and R. Tenne, *Macromol. Chem. Phys.*, 2013, **214**, 2007–2015.
- 57 P. Bhattacharya, *Semiconductor optoelectronic devices*, Prentice-Hall, Inc., USA, 2nd edn, 1997.
- 58 J. P. Banerjee and S. Banerjee, *Physics of Semiconductors and Nanostructures*, CRC Press, 2019.
- 59 A. Kumar, K. Intonti, L. Viscardi, O. Durante, A. Pelella, O. Kharsah, S. Sleziona, F. Giubileo, N. Martucciello, P. Ciambelli, M. Schleberger and A. Di Bartolomeo, *Mater. Horiz.*, 2024, **11**, 2397–2405.
- 60 A. Grillo, E. Faella, A. Pelella, F. Giubileo, L. Ansari, F. Gity, P. K. Hurley, N. McEvoy and A. Di Bartolomeo, *Adv. Funct. Mater.*, 2021, **31**, 2105722.
- 61 R. A. Evarestov, A. V. Bandura, V. V. Porsev and A. V. Kovalenko, *J. Comput. Chem.*, 2017, **38**, 2581–2593.
- 62 K. K. Kam and B. A. Parkinson, *J. Phys. Chem.*, 1982, **86**, 463–467.

